



SAPIENZA  
UNIVERSITÀ DI ROMA

DEPARTMENT OF PHYSICS

# Neutron Activation Analysis

## PHYSICS LABORATORY II

**Professors:**

Gianluca Cavoto

Salvatore Fiore

**Students:**

Giovanni Necci

1767839

Giovanni Luca Pesce

1757232

Nikola Prodanov

1768690

---

Academic Year 2021/2022

# Contents

<b>1</b>	<b>Introduction</b>	<b>3</b>
<b>2</b>	<b>HPGe Detector</b>	<b>4</b>
2.1	Calibration . . . . .	4
2.2	Efficiency . . . . .	6
2.2.1	Efficiency with 10 cm of thickness . . . . .	7
2.2.2	Efficiency with 6 cm of thickness . . . . .	8
<b>3</b>	<b>Neutron Flux Measurements</b>	<b>10</b>
3.1	Neutron Activation Analysis . . . . .	12
3.1.1	Experimental Setup . . . . .	12
3.1.2	Measurements . . . . .	12
<b>4</b>	<b>Attenuation Coefficient</b>	<b>17</b>
4.1	Strategy of measurement . . . . .	17
4.2	Results . . . . .	18
<b>5</b>	<b>Neutron Flux Distribution</b>	<b>21</b>
5.1	The experimental setup . . . . .	21
5.2	Results . . . . .	22
<b>6</b>	<b>FNG</b>	<b>23</b>
6.1	Neutron Activation Analysis . . . . .	25
6.1.1	Measurements . . . . .	25
<b>7</b>	<b>Conclusions</b>	<b>28</b>
<b>8</b>	<b>Appendix</b>	<b>29</b>
8.1	Energy peaks . . . . .	29
8.2	Evaluation of Efficiency . . . . .	31
8.3	Effective Cross Section . . . . .	32
8.3.1	Thermal Cross Section . . . . .	32
8.3.2	Fast Cross Section . . . . .	33

<b>9</b>	<b>Tables</b>	<b>34</b>
<b>10</b>	<b>Glossary</b>	<b>38</b>
	<b>Bibliography</b>	<b>39</b>

# Chapter 1

## Introduction

The aim of this paper is to discuss the experimental methods of neutron activation, in our case carried out using two different neutron sources: an *Americium-Berillium* source and the *Frascati Neutron Generator*. 14 MeV FNG, designed and built at ENEA in Frascati, is based on the fusion reaction  $T(d;n)\alpha$  and produces up to  $10^{11}n/s$  continuously or pulsed.

First we have calibrated the HPGe detector, which is a semiconductor detector used for activity measurements, through the decay scheme of known isotopes.

Subsequently we measured its efficiency at different heights, comparing the number of particles counted by the detector to the number of particles theoretically expected from the surface of detection.

Afterwards, we estimated the neutron flux of an *AmBe* source, analyzing two foils:  $^{197}\text{Au}$  and  $^{115}\text{In}$ . They were put in the reaction chamber so that the neutron flux is orthogonal to the surface of the foils.

Then we estimated the attenuation coefficient of a specific element,  $^{116m}\text{In}$ , through 9 configuration obtained with 4 kind of Indium foils of different mass and thickness. We also found out that for thin foils the self attenuation coefficient is negligible.

Afterwards we measured the surface flux distribution, from an *AmBe* source that emits thermal neutrons at a fixed distance, on five thin foils of  $^{197}\text{Au}$  symmetrically distributed on a flat surface.

Finally, we used FNG, knowing its technical details, to analyze and determinate two unknown isotopes, by the analysis of the Gamma spectrum, and consequently the evaluation of the total flux which hit the two samples.

Data analysis throughout this paper is done with Python3 [1] and in the last chapter called "Appendix" there are some explanations about some experimental procedures.

# Chapter 2

## HPGe Detector

### 2.1 Calibration

As said in the introduction, the first part of the experience focused on the calibration of the HPGe Detector which will be used for activated samples measurements. Compared to silicon detectors, germanium is much more efficient than silicon for radiation detection due to its atomic number (32) being much higher than silicon (14), and lower average energy necessary to create an electron-hole pair, which is 3.6  $eV$  for silicon and 2.9  $eV$  for germanium. Moreover we also have advantages regarding the energy resolution: the FWHM in germanium detectors is a function of energy. For a 1.3  $MeV$  photon, the Breit-Wigner FWHM, describing the resonance peak, is 2.1  $keV$ , which is very low. [2]

The simplest and most effective way to calibrate, it is to analyze the gamma spectrum of some known samples. Knowing the decay scheme of the foil, it is possible to associate the theoretical energy value of the emitted photon to each channel identified by the peak of counts. This analysis is possible via a software [3], related with the detector, able to reconstruct the gamma spectrum.

For our purpose we analyzed the following samples:  $^{60}Co$ ,  $^{137}Cs$ ,  $^{152}Eu$ ,  $^{133}Ba$ .

A very important factor to take in account for this measurements is represented by the background noise. Before any kind of detection, an "empty" measurement was carried out for about 30 minutes in order to subtract it from the one with the known sample. In Figure 2.1 there is an example of a detected spectra of cosmic rays.

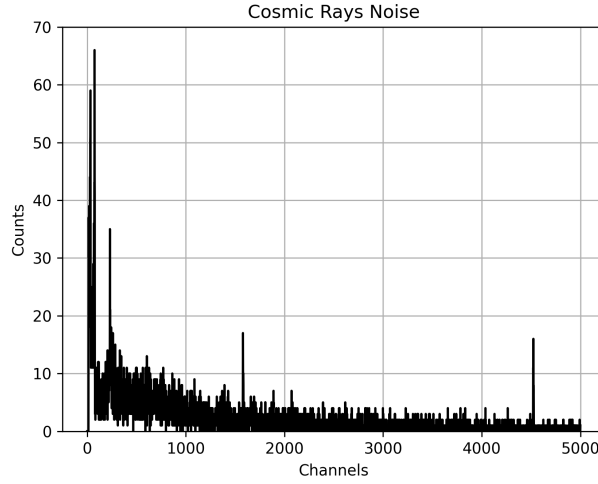


Figure 2.1: Cosmic background noise acquired for 30 minutes

The main goal is to find the conversion factor between channel and energy featured by the angular coefficient of the regression line of these 2 variables. In such a way to do that we extracted every spectrum provided from the software and analyzed each peak. For every single peak, a gaussian fit was made in order to extract the exact value of the channel (for the details of this method, see section 8.1 of chapter 8). Taking into account all the values of the channels we plotted the channel versus the theoretical energy of each peak.

The result is in Figure 2.2.

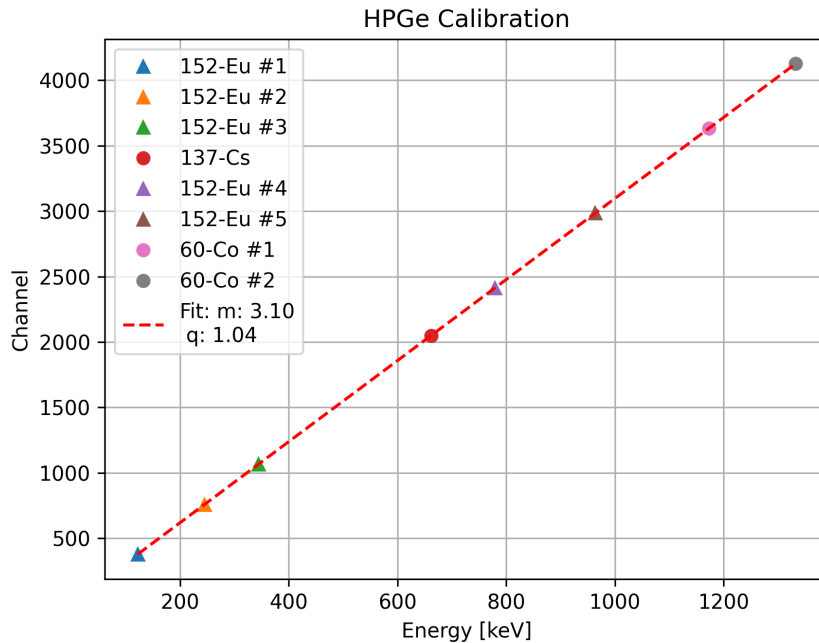


Figure 2.2: Channel Vs Energy peaks distribution. The parameter  $m$  of the fit represents the conversion factor between the 2 variables.

For an additional check of the conversion value, we also focused on the energy range 0-500 *KeV* using *Europium* and *Barium* peaks only, in order to prove the real linear trend and to avoid the overlaps of too many points. Results are shown below in Figure 2.3.

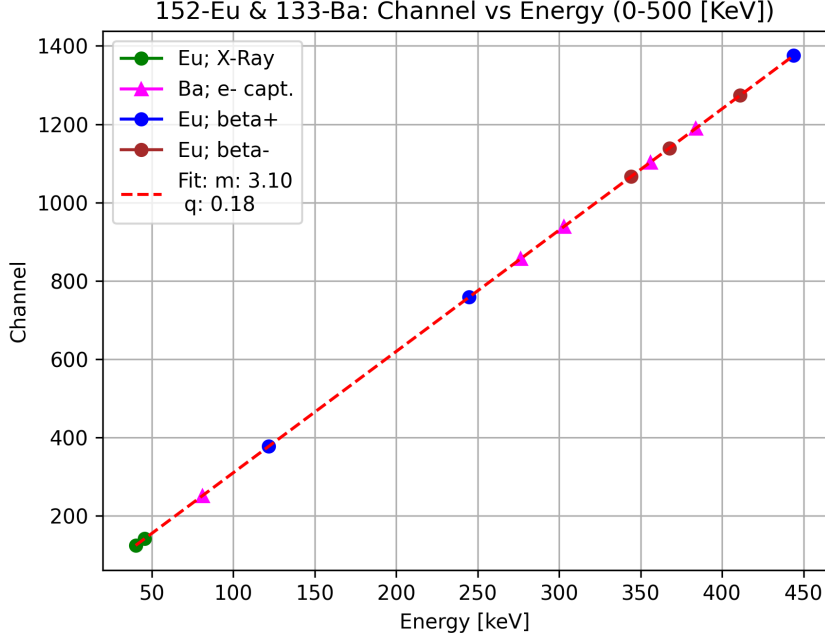


Figure 2.3: Channel Vs Energy peaks distribution for  $^{133}\text{Ba}$  and  $^{152}\text{Eu}$  in the energy range 0-500 *KeV*. In the legend is indicated, for each peak, the kind of decay.

As reported in the legend of Figure 2.3, the parameter  $m$  of the fit is equal to the one in Figure 2.2. Therefore it's possible to establish the following relation:

$$\text{Channel} = 3.1 * \text{Energy} \quad (2.1)$$

## 2.2 Efficiency

Once the HPGe detector was calibrated, we proceeded to test its efficiency. In principle efficiency is the *per-event* probability to detect the particle. In other words, in the case of particle detection, it's the ratio between the number of particles actually counted by the detector and the number of particles which are expected to be counted: we call this quantity  $\epsilon = \frac{n}{N} = \frac{N_{\text{measured}}}{N_{\text{emitted}}}$ . [4]

Given  $N$  particles passing through the detector, the probability to see  $n$  particles follows a binomial distribution:

$$p(n) = \binom{N}{n} p^n (1-p)^{N-n} \quad (2.2)$$

with an expected value and an uncertainty equal to:

$$\mu = Np = n \quad (2.3)$$

$$\sigma_n = \sqrt{Np(1-p)} \quad (2.4)$$

The variance of the efficiency is

$$\sigma_\epsilon^2 = \frac{\sigma_n^2}{N^2} = \frac{Np(1-p)}{N^2} = \frac{\epsilon(1-\epsilon)}{N} \quad (2.5)$$

hence it follows that:

$$\epsilon \pm \sigma_\epsilon = \frac{n}{N} \pm \sqrt{\frac{\epsilon(1-\epsilon)}{N}} \quad (2.6)$$

In our case we have:

$$\epsilon = \frac{N_{measured}}{N_{emitted}} = \frac{N_{measured}}{AY\Delta t} \quad (2.7)$$

where:  $A$  is the current activity of the sample, indeed knowing the value  $A_0$  at a certain time we readjusted that value with a new one given by the exponential decay law  $A(t) = e^{-\frac{t}{\tau}}$ , where  $\tau$  is the mean lifetime;  $Y$  is the *yield* (intensity) of a peak which is linked to the Branching Ratio of the sample's decay;  $\Delta t$  is the measurement time;  $N_{measured}$  are the counts measured for each peak (for the details on how they were measured see section 8.2 of chapter 8). All the values of  $Y$  were obtained by the *LBNL Nuclear Data Search* [5]

### 2.2.1 Efficiency with 10 cm of thickness

Via the use of Equation 2.7 we tested the efficiency of the detector with, separately, two samples of  $^{152}\text{Eu}$  and  $^{133}\text{Ba}$  placed 10 cm away from the support surface of the detector.

Computed data are contained in Table 9.1. The plot of the efficiency at 10 cm of thickness is shown in Figure 2.4:



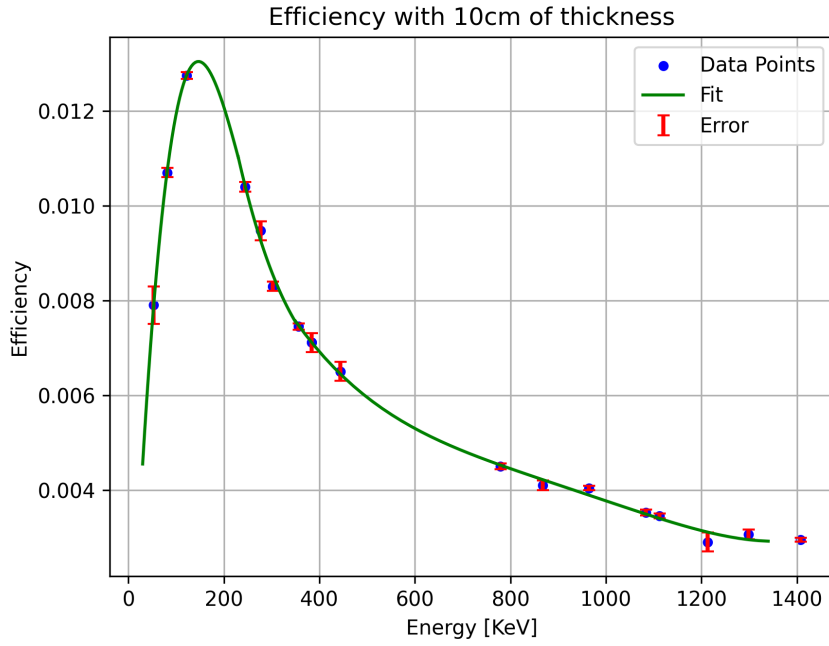


Figure 2.4: Efficiency Vs Energy obtained by two samples of  $^{152}\text{Eu}$  and  $^{133}\text{Ba}$  placed 10 cm away from the support surface of the detector. To approximate as best as possible data's trend, points are interpolated with a polynomial fit.

### 2.2.2 Efficiency with 6 cm of thickness

An analogous test was done with the same two samples which were located, this time, at a distance of 6 cm from the support surface.

Computed data are contained in Table 9.2. The plot of the efficiency with 6 cm of thickness is shown in Figure 2.5:

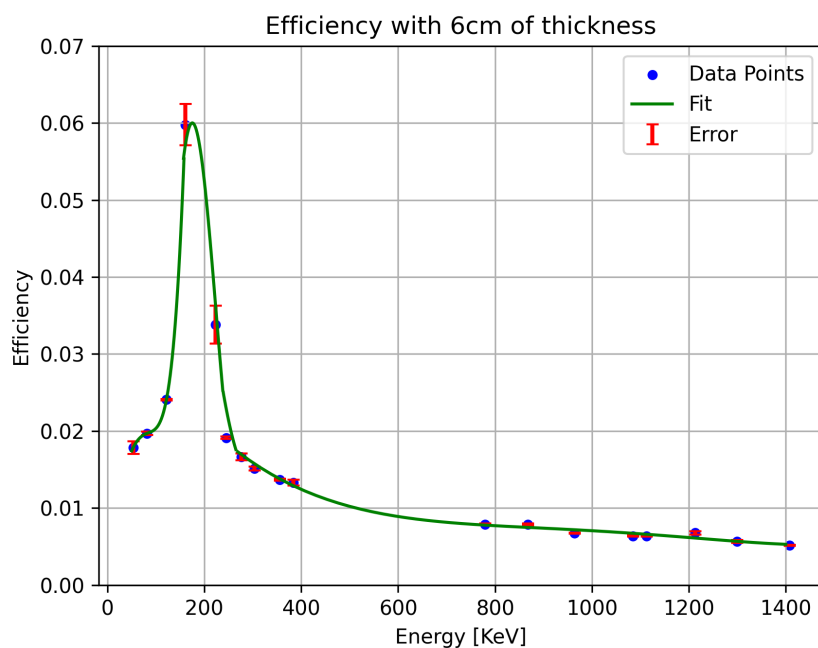


Figure 2.5: Efficiency Vs Energy obtained by two samples of  $^{152}\text{Eu}$  and  $^{133}\text{Ba}$  placed 6 cm away from the support surface of the detector. To approximate as best as possible data's trend, points are interpolated with a polynomial fit.

# Chapter 3

## Neutron Flux Measurements

In this section we will analyze one of the most characterizing topics of the entire report: the neutron flux to which a sample has been exposed. The neutron flux is made up of thermal neutrons and fast neutrons. Thermal neutrons, or slow neutrons, have kinetic energy of the order of few electronvolts or a fraction of electronvolt.

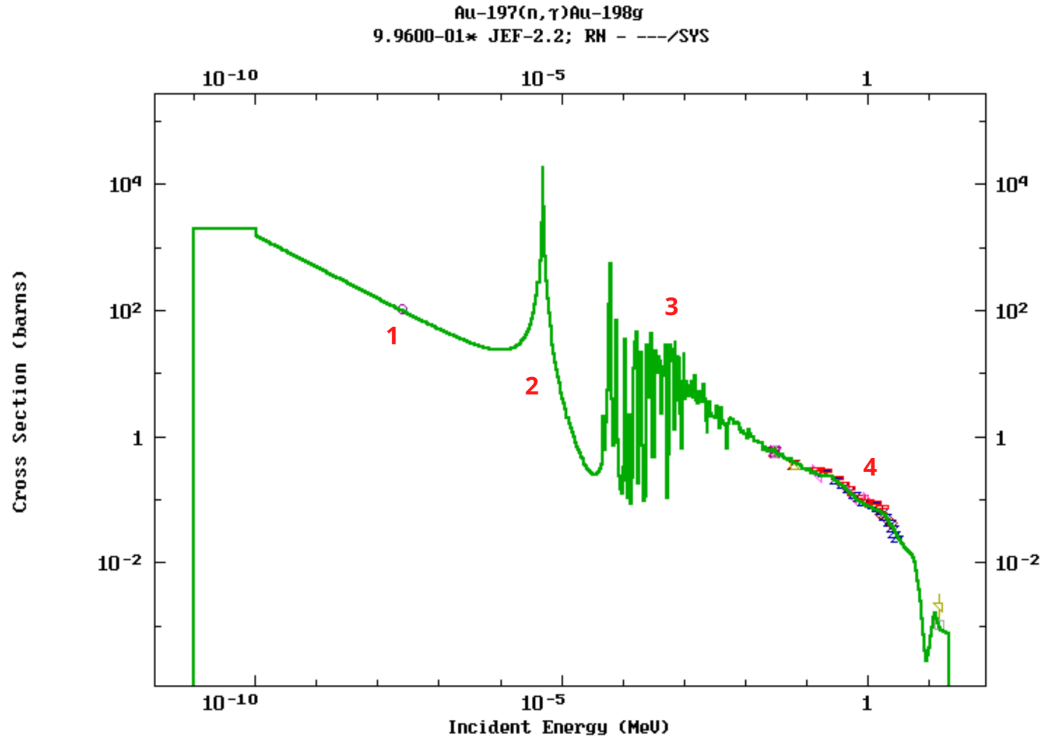


Figure 3.1: Cross Section VS Incident Energy for the nuclear reaction  $^{197}\text{Au}(n, \gamma)^{198}\text{Au}$ . We can distinguish 4 regions depending on the incident neutron energy: **1**) Thermal region; **2**) Neutron capture region. At low energies the cross section of this process has the typical trend  $\frac{1}{\sqrt{E}}$ ; **3**) Resonance region. This multitude of resonances is due to the formation of the new nucleus; **4**) Fast region. This plot was taken from the Database [6]

When the neutron energy becomes comparable to the kinetic energies of the atoms  $E_K = k_B T = 0.025$  eV belonging to the medium through which they travel, the neutrons are said thermal. Meanwhile fast neutrons, which are produced by fission reactions, usually have energies between 1 MeV and 2 MeV.

Different energy neutrons will have different reactions with atoms, therefore a different cross section. An example of a neutron cross section as a function of energy can be seen in 3.1. It's no coincidence that we have shown this graph as an example, we will need it for many measurements that we will carry out later.

In general the reaction rate of particles hitting on a target will be given by:

$$\lambda = \sigma \phi \quad (3.1)$$

Where  $\sigma$  is the cross section and  $\phi$  is the flux of the particles. If the flux is made up of different energy particles the rate of reaction will be:

$$\lambda = \int_0^\infty dE \sigma(E) \tilde{\phi}(E) \quad (3.2)$$

Where  $\tilde{\phi}(E)$  is the distribution of the flux as a function of energy (for example: if the flux is made up of particles with fixed energy  $E_0$ , then the flux distribution as a function of energy will be  $\tilde{\phi}(E) = \delta(E - E_0)\phi$ ). Since Figure 3.1 shows us that the  $\sigma(E)$  is noticeably different in the region of thermal and fast neutrons, we will approximate the total flux of neutrons  $\phi_{tot}$  as a sum of the thermal flux  $\phi_{th}$  and the fast flux  $\phi_f$ :

$$\phi_{tot} = \phi_{th} + \phi_f \quad (3.3)$$

We can totally neglect the contribution of regions **2** and **3** for flux measurements, because we knew *a priori* that the neutron flux was made up of only thermal and fast neutrons. Overall is very hard to estimate, for the above cited regions, a coherent value of  $\sigma$ . For simplicity we did a further approximation of the cross section energy distribution: we introduce the effective cross section as the expected value of  $\sigma(E)$  in the domain of each energy regions. In our case we obtain two effective cross sections, one for the thermal region  $\sigma_{th}$  and the other for the fast region  $\sigma_f$  (see section 8.3). Using these approximations and equations 3.2 and 3.1, the rate of neutron reaction  $\lambda_n$  becomes:

$$\lambda_n = \sigma_{th}\phi_{th} + \sigma_f\phi_f \quad (3.4)$$

These approximations can be generalised to all elements.

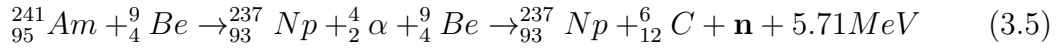
So far we have seen that, if we find the rate reaction  $\lambda_n$ , we can obtain the neutron flux. In the next section we will show the experimental setup and how we measured the rate of neutron reaction with different elements.

## 3.1 Neutron Activation Analysis

As said, a sample has been **activated** by neutron exposure, if at least one atom belonging to the sample has changed its internal nuclear structure. Therefore the neutron activations of any element might have created some isomers or elements that started a chain reaction of decay. Typically these decays have the spectrum of gamma energy photons which we can easily detect with our HPGe detector.

### 3.1.1 Experimental Setup

For the neutron activation analysis (NAA) we used two foils, one made of pure *Gold*  $^{197}\text{Au}$  and the other of pure *Indium*  $^{115}\text{In}$  with the following mass values:  $m_{\text{Au}} = 1,47\text{g}$ ,  $m_{\text{In}} = 14,85\text{g}$ . Both of the foils were put in the reaction chamber in such a manner that the direction of the neutron flux is orthogonal to the surfaces of  $^{197}\text{Au}$  and  $^{115}\text{In}$ . The source which generates neutrons is an alloy of  $^{241}\text{Am}$  oxide ( $\text{Am}_2\text{O}_3$ ) and metallic  $^9\text{Be}$ . In the reaction, the neutron is emitted, following absorption by a *Beryllium* nucleus (target) of an  $^4_2\alpha$  particle (projectile) obtained by decay of the  $^{241}\text{Am}$ . The reaction which produces the neutron is the following:



### 3.1.2 Measurements

The foils were exposed on the 9<sup>th</sup> May 2022 at 15:45 and were taken out the following day at 14:10. We redefine the time reference so that the start of the exposure is at  $t = 0$ , the end of the exposure is at  $T = 22\text{h}25\text{min}$  and the time of the gamma spectrum analysis with the HPGe of the activated  $i$ -th element as  $t_i$ . For Gold and Indium we have  $t_{\text{Au}} = 23\text{h}26\text{min}$  and  $t_{\text{In}} = 23\text{h}50\text{min}$ .

In our analysis we take in account that the activated elements start decaying at the moment they are created during the neutron exposure and also after taking them out of the reactor after times  $t > T$ .

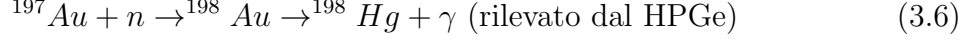
We can identify the new elements/isomers created after the exposure by analysis of the gamma-ray energy spectrum produced in the HPGe detector. In the next two subsections is described the Neutron Activation Analysis for both samples.

#### NAA for gold $^{197}\text{Au}$

The gamma spectroscopy of the activated Gold foil showed us only one peak at  $411\text{ keV}$  which could only corresponds to the gamma photon from the decay:  $^{198}\text{Au} \rightarrow ^{198}\text{Hg} + \gamma$ , with a decay constant:  $\lambda_{\tau}^{198\text{Au}} = 0,0107\text{h}^{-1}$ . We label the decay constant with a lower index  $\tau$  meanwhile the rate of activation with neutrons will is

labeled with a lower index  $n$ .

The complete reaction of activation and decay is:



For times  $0 < t < T$ , during the activation process, the number of elements are determined by the following laws:

$$\begin{aligned} \dot{N}^{197\text{Au}}(t) &= -\lambda_n^{197\text{Au}} N^{197\text{Au}}(t) & \text{with } N^{197\text{Au}}(0) &= N^{\text{Au}} \\ \dot{N}^{198\text{Au}}(t) &= \lambda_n^{197\text{Au}} N^{197\text{Au}}(t) - \lambda_\tau^{198\text{Au}} N^{198\text{Au}}(t) & \text{with } N^{198\text{Au}}(0) &= 0 \end{aligned}$$

Where  $N^{\text{Au}}$  is the number of atoms of  $\text{Au}$ , i.e.  $N^{\text{Au}} = \frac{\text{Total mass}}{\text{mass of a single atom}}$ . Meanwhile for times  $t > T$ , after the activation process, the number of elements are determined by:

$$\begin{aligned} \dot{N}^{197\text{Au}}(t) &= 0 & \text{with } \lim_{t \rightarrow T^+} N^{197\text{Au}}(t) &= \lim_{t \rightarrow T^-} N^{197\text{Au}}(t) \\ \dot{N}^{198\text{Au}}(t) &= -\lambda_\tau^{198\text{Au}} N^{198\text{Au}}(t) & \text{with } \lim_{t \rightarrow T^+} N^{198\text{Au}}(t) &= \lim_{t \rightarrow T^-} N^{198\text{Au}}(t) \end{aligned}$$

Inside of the HPGe detector, we measure the activity of  $^{198}\text{Au}$ , that means we are only interested in:

$$A(^{198}\text{Au}) = \left| \frac{\Delta N^{198\text{Au}}}{\Delta t_{\text{Au}}} \right| = \left| \frac{N^{198\text{Au}}(t_{\text{Au}} + \Delta t_{\text{Au}}) - N^{198\text{Au}}(t_{\text{Au}})}{\Delta t_{\text{Au}}} \right| \quad (3.7)$$

Where  $t_{\text{Au}}$ , as defined, is the time of the gamma spectrum analysis with the HPGe of the activated  $\text{Au}$  and  $\Delta t_{\text{Au}}$  is the time duration of the activity measurement in the HPGe detector. Since  $\lambda_\tau^{198\text{Au}} \Delta t_{\text{Au}} \ll 1$ , we may consider  $\Delta t_{\text{Au}}$  as an infinitesimal, so that the right hand expression inside the modulus of 3.7 becomes, by definition, a derivative at time  $t_{\text{Au}}$ :

$$A^{198\text{Au}}(t) = \left| \dot{N}^{198\text{Au}}(t) \right|_{t=t_{\text{Au}}} \quad (3.8)$$

The laws of time decay and neutron activation give the final expression, for time  $t > T$ :

$$A^{198\text{Au}}(t) = \left| \frac{\lambda_\tau^{198\text{Au}}}{\lambda_\tau^{198\text{Au}} - \lambda_n^{197\text{Au}}} \lambda_n^{197\text{Au}} N^{\text{Au}} (e^{-\lambda_n^{197\text{Au}}T} - e^{-\lambda_\tau^{198\text{Au}}T}) e^{-\lambda_\tau^{198\text{Au}}(t-T)} \right| \quad (3.9)$$

In general one cannot find an analytical expression for  $\lambda_n^{197\text{Au}}$ , the best approach is by solving it with numerical computation, but in some cases approximations give clear results. We can further simplify this expression with the following consideration: using 3.1 and Figure 3.1 we can estimate the expected value of the rate of activation of  $\lambda_n^{197\text{Au}}$ . We see that the highest value of the cross section is  $\sigma \sim 10^3$  barn and the neutron total flux has to be lower than  $\phi \sim 10^{12} \text{ cm}^{-2}\text{s}^{-1}$ . This tells us that  $\lambda_n^{197\text{Au}} < 10^{-6} \text{ h}^{-1}$ . In other words:

$$\lambda_\tau^{198\text{Au}} \gg \lambda_n^{197\text{Au}} \quad (3.10)$$

This simplifies the expression 3.9 and gives the final result for the rate of neutron activation as a function of the measured activity and different parameters:

$$\lambda_n^{197\text{Au}} = \frac{A^{198\text{Au}}(t)}{N^{\text{Au}}} \frac{e^{\lambda_\tau^{198\text{Au}}(t-T)}}{1 - e^{-\lambda_\tau^{198\text{Au}}T}} \quad (3.11)$$

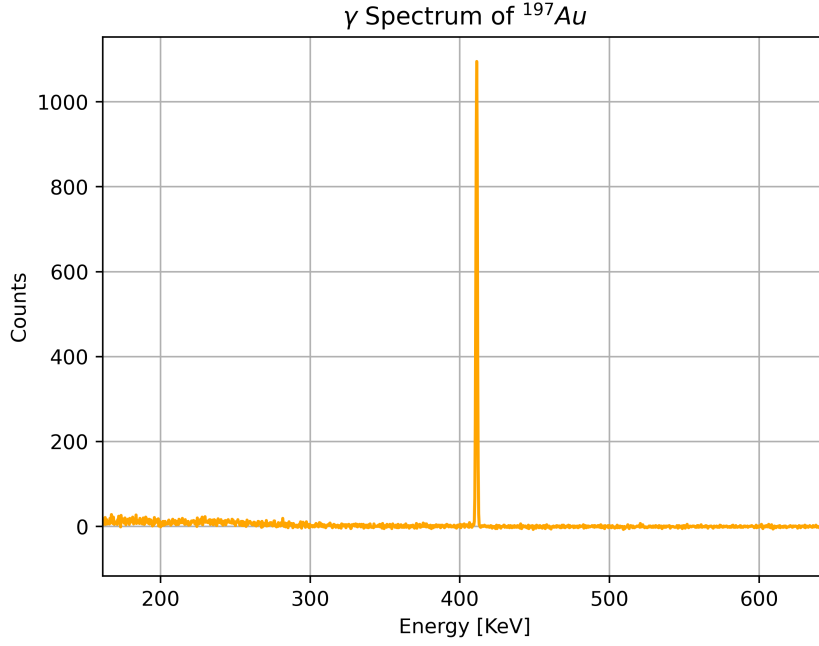


Figure 3.2: Gamma spectrum of <sup>197</sup>Au in the relevant energy range 100 ÷ 650 keV.

These kind of approximations can be used in several cases of NAA.

We measured the Activity with the HPGe by inverting 2.7 to obtain:

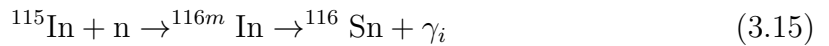
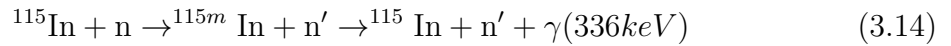
$$A^{197Au}(t_{Au}) = (530 \pm 20) Bq \quad (3.12)$$

Taking this result and inserting it in 3.11 we obtain a result for the rate of activation of neutrons with <sup>197</sup>Au to be:

$$\lambda_n^{197Au} = (5.8 \pm 0.2) \cdot 10^{-19} s^{-1} \quad (3.13)$$

### NAA for indium <sup>115</sup>In

The NAA for indium is slightly different from that one of gold. The gamma spectroscopy of <sup>115</sup>In (see 3.1) showed us that the new formed elements are <sup>115m</sup>In and <sup>116m</sup>In. Where the index *m* stands for metastable element - different rearengement of nucleides in the nucleus. The only possible reactions for the formation of these new elements are:



Where  $\gamma_i$  in 3.15 represents all the different gamma peaks measured. These two reactions (3.14 and 3.15) happen simultaneously in the time  $0 < t < T$  during the neutron exposure. After which, the metastable elements start immediately decaying with decay constants  $\lambda_\tau^{115mIn} = 0.154h^{-1}$  and  $\lambda_\tau^{116mIn} = 0.766h^{-1}$ . We can represent

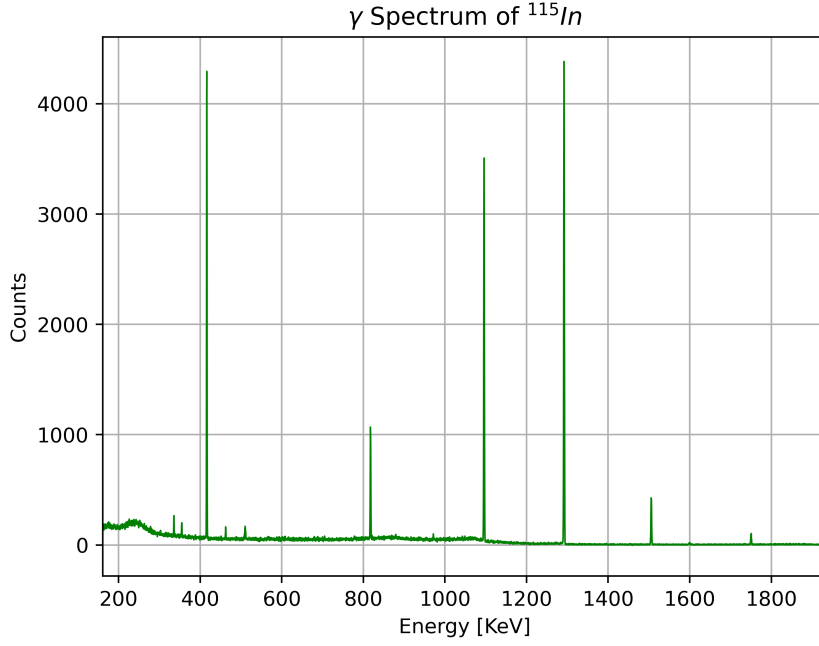
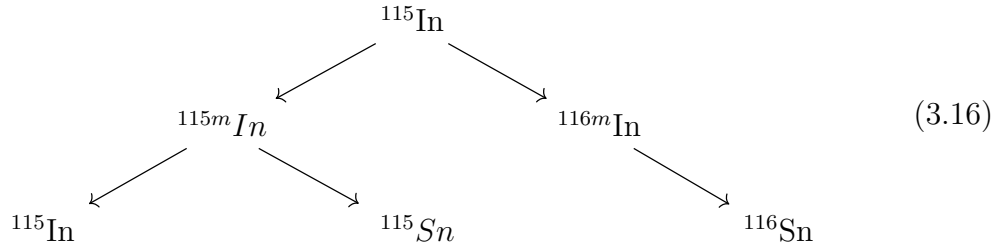


Figure 3.3: Gamma spectrum of  $^{115}\text{In}$  in the relevant energy range  $100 \div 2000 \text{ keV}$ .

the complete chain reaction as:



As we did in the NAA for gold, the numbers of each interested elements, for times  $0 < t < T$  are determined by:

$$\begin{aligned}
 \dot{N}^{115\text{In}}(t) &= -(\lambda_n^{115m\text{In}} + \lambda_n^{116m\text{In}})N^{115\text{In}}(t) + \lambda_\tau^{115m\text{In}}N^{115m\text{In}}(t) \quad \text{with } N^{115\text{In}}(0) = N^{\text{In}} \\
 \dot{N}^{116m\text{In}}(t) &= \lambda_n^{116m\text{In}}N^{115\text{In}}(t) - \lambda_\tau^{116m\text{In}}N^{116m\text{In}}(t) \quad \text{with } N^{116m\text{In}}(0) = 0
 \end{aligned}$$

Neglecting the term of recreation of  $^{115}\text{In}$  after the decay from  $^{115m}\text{In}$ , we obtain the activity to be, for times  $t > T$ :

$$A^{116m\text{In}}(t) = \frac{\lambda_\tau^{116m\text{In}} \lambda_n^{116m\text{In}} N^{\text{In}}}{\lambda_\tau^{115m\text{In}} - \lambda_n^{115m\text{In}} - \lambda_n^{116m\text{In}}} (e^{-(\lambda_n^{115m\text{In}} - \lambda_n^{116m\text{In}})T} - e^{\lambda_\tau^{116m\text{In}}T}) e^{-\lambda_\tau^{116m\text{In}}(t-T)} \tag{3.17}$$

Using the same deduction as we did in the NAA for Gold, we obtain the same expression as we did in 3.11 for the rate of activation of  $\lambda_n^{116m\text{In}}$ . Taking the measured activities from the gamma peaks (see table 3.1) we find the rate of neutron activation to be:

$$\lambda_n^{116m\text{In}} = (3.6 \pm 0.2) \cdot 10^{-19} \text{ s}^{-1} \tag{3.18}$$



Element	Energy[keV]	Gamma Yield	Activity[kBq]	$\sigma(\text{Activity})[\text{kBq}]$
$^{116m}\text{In}$	416	0.277	9.3	0.5
$^{116m}\text{In}$	1097	0.562	9.6	0.6
$^{116m}\text{In}$	1293	0.844	9.5	0.6
$^{116m}\text{In}$	1507	0.10	9.2	0.5
$^{116m}\text{In}$	1752	0.025	9.2	0.5

Table 3.1: Gamma spectroscopy analysis with the HPGe of the activated Indium-115 foil. The peaks with the highest gamma yields are only shown.

### The total flux

Having measured the rate of neutron activation, it is possible to find the neutron fluxes from 3.4. In our case we obtain three different equations for two unknowns  $\phi_{th}$  and  $\phi_f$ :

$$\begin{aligned}\lambda_n^{197Au} &= \sigma_{th}^{197Au} \phi_{th} + \sigma_f^{197Au} \phi_f \\ \lambda_n^{116mIn} &= \sigma_{th}^{116mIn} \phi_{th} + \sigma_f^{116mIn} \phi_f\end{aligned}$$

The cross sections are given in table 3.2. We obtain that the thermal flux, fast flux and the total flux are:

$$\begin{aligned}\phi_{th} &= (5.5 \pm 0.3) \cdot 10^3 \text{cm}^{-2} \text{s}^{-1} \\ \phi_f &= (4.9 \pm 0.3) \cdot 10^5 \text{cm}^{-2} \text{s}^{-1}\end{aligned}$$

Cross section	$^{197}\text{Au}$	$^{115}\text{In}$
$\sigma_{th}[\text{barns}]$	$98 \pm 2$	$45 \pm 2$
$\sigma_f[\text{barns}]$	$0.08 \pm 0.005$	$0.16 \pm 0.01$

Table 3.2: Cross sections for neutron activation for Gold and Indium in the fast and thermal regime, to see how they have estimated check 8.3.

# Chapter 4

## Attenuation Coefficient

The main goal of this part of the experience is to estimate the  $\gamma$ -ray attenuation coefficient of a specific element.

The attenuation coefficient characterizes how easily a volume of material can be penetrated by a beam of  $\gamma$ . A beam of monoenergetic photons with an incident intensity  $I_0$ , penetrating a layer of material with mass thickness  $x$  and density  $\rho$ , emerges with intensity  $I$  given by the exponential attenuation law:

$$I(x) = I_0 e^{-\left(\frac{\mu}{\rho}\right)x} \quad (4.1)$$

Having available multiple *Indium* ( $^{116m}\text{In}$ ) foils of different thickness, and therefore mass, we performed measurements with the HPGe using different configurations.

### 4.1 Strategy of measurement

Specifically there were 4 kind of *Indium* foils which we denote as: *thin, medium, thick A, thick B*. In Table 9.3 we report the features of each sample. Here is the list of the configurations:

1. *Thin*
2. *Medium*
3. *Thick B*
4. *Thick A*
5. *Thin + thick A*
6. *Medium + thick A*
7. *Thick A + thick B*
8. *Thin + thick A + thick B*

### 9. *Medium + thick A + thick B*

The values of mass and thickness were respectively measured with a digital scales and with a centesimal calipers. Let's make a briefly digression on the related errors. For the digital scales we assume a uniform distribution of the read values within the resolution range (equal to 0,01), therefore for the mass we consider an error equal to:

$$\sigma_{mass} = \frac{0,01}{\sqrt{12}} \simeq 0,003 \quad (4.2)$$

For the centesimal calipers we have a resolution of 0,01 *mm*. We performed 5 measurements for each sample (the mean values are the ones reported in Table 9.3), and we have estimated the error as the standard deviation of the values. For all the four samples we have an error of the thickness equal to:

$$\sigma_{thickness} \simeq 0,001 \quad (4.3)$$

Both the errors are negligible compared to the values.

All the measurements acquired from the 9 configurations cited above, have been made with a mount of 6 *cm* in order to put the *Indium* samples at a distance, of this amount, from the support surface. As usual, a background noise measurement of 30 minutes was made, in order to subtract it from the actual measurements.

Extrapolating the value of the efficiency at a certain energy from the plot 2.5 and inverting the relation 2.7, it's possible to obtain the total activity. Thereafter, normalizing the activity with respect to the mass, via equation 4.1 is feasible to extract the value of attenuation coefficient  $\mu$  by fitting the data.

## 4.2 Results

Figure 4.1 shows the trend of the total activity normalized with respect to the total mass for four different values of  $^{116m}In$  energy peaks. In Table 9.4 are reported all the values of the plot.

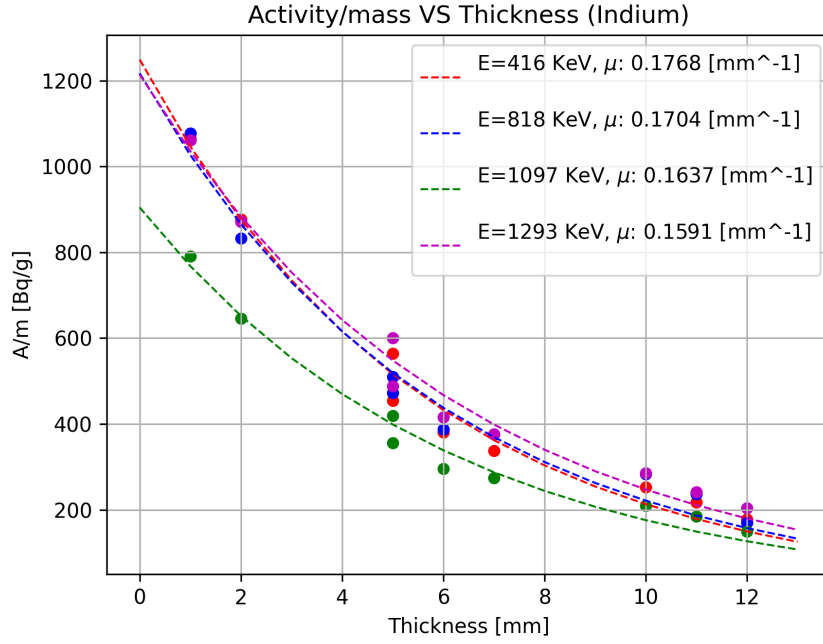


Figure 4.1: *Activity/Mass VS Thickness* for 4 energy peaks of 9 *Indium* sample's configurations. Different colors refer to different energy peak.

As said at the end of Section 4.1, an exponential fit of the data was made, in order to extrapolate parameter values, including  $\mu$ . In the legend of Figure 4.1, the values of  $\mu$  are reported for each energy peak. We show in Table 9.5 the  $\mu$  values with the corresponding errors. Said errors are estimated from the covariance matrix through the fit algorithm [1].

Moreover, it's interesting to see the trend of the *mass absorbtion coefficient* related to each energy peak described for Figure 4.1. The *mass absorbtion coefficient* ( $\frac{\mu}{\rho}$ ) is the proportion of initial photon energy that is locally transferred to the material through ionization and excitation [7]. Therefore, assuming an average density of  $^{116m}\text{In}$  equal to  $\rho_{\text{In}} = 7,31[\frac{\text{g}}{\text{cm}^3}]$ , we report in Figure 4.2 the above-mentioned trend.

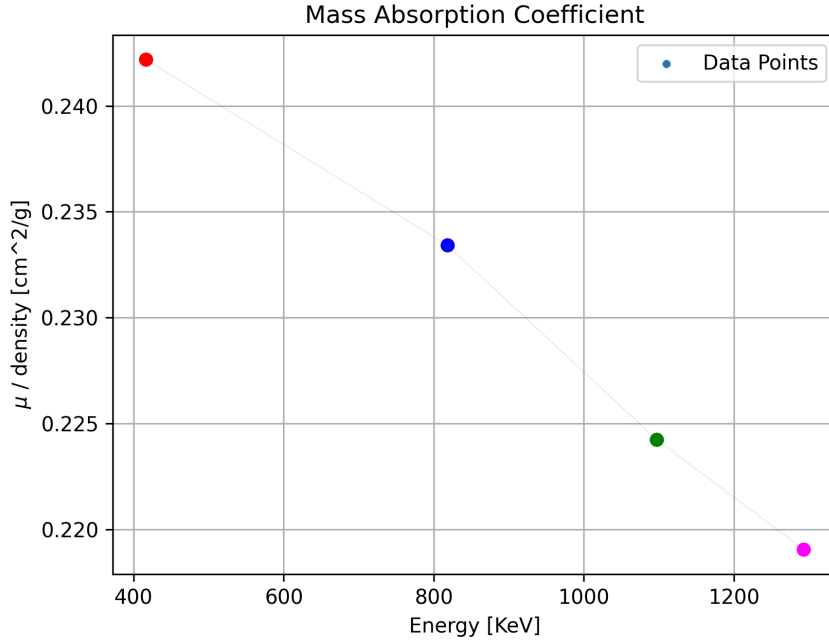


Figure 4.2: Absorption coefficient normalized with respect to Indium density VS Energy

The trends of Figures 4.1 and 4.2, and  $\mu$  values of Table 9.5 as well, were compared with those of the NIST database [8]. Both are in agreement with the database's data.

Once the values of  $\mu$  for a specific energy are estimated, we can now introduce an important quantity: the self attenuation correction factor. The general formula of this quantity (4.4) takes in account: the attenuation coefficient  $\mu$  of the sample material for the energy  $E$ ; the trajectory through the sample  $e$ ; the transmission  $T$  through the absorber; the probability  $P$  of full-energy absorption in the detector.

$$C_{att} = \frac{\int_V dV \int_{\Omega} e^{(-\mu(E) \cdot e(\vec{r}, \vec{t}))} \cdot T(e, \vec{r}, \vec{t}) \cdot P(e, \vec{r}, \vec{t}) \cdot d\Omega}{\int_V dV \int_{\Omega} T(e, \vec{r}, \vec{t}) \cdot P(e, \vec{r}, \vec{t}) \cdot d\Omega} \quad (4.4)$$

In case the sample is near the detector, 4.4 can be simply rewritten as:

$$C_{att} = \frac{1 - e^{-\mu x}}{\mu x} \quad (4.5)$$

From the results obtained before, it turns out that this correction factor must be taken into account at low energies and when the thickness of the sample increases. This is a very important starting point for what we are going to discuss in the next chapter.

# Chapter 5

## Neutron Flux Distribution

In this section we measured the surface flux distribution of a neutron beam composed of thermal neutrons at a fixed distance. We recall that thermal neutrons have a kinetic energy of 0,025 eV. Essentially we want to know if the flux is homogeneous or heterogeneous and if it has any dependence on the angle  $\theta$  and the radial distance  $r$  on the surface.

### 5.1 The experimental setup

We made a surface disc of a diameter  $d = 28cm$  on which we labeled the distances from the center every  $45^\circ$ . Having 5 Golden  $^{197}Au$  samples, labeled with  $i = 1, \dots, 5$  of radius  $r_i = 5mm$  and different masses  $m_i$ , we place them in the following manner (see Figure 5.1) to define also a polar coordinate system  $(r, \theta)$  as in table 9.6

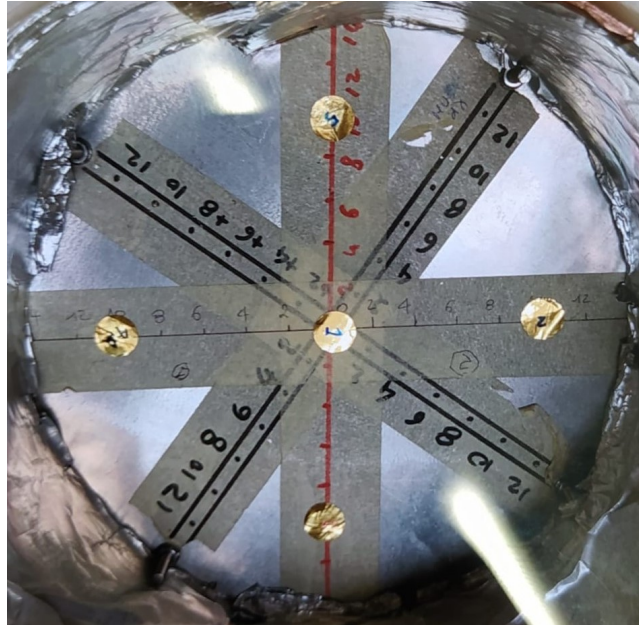


Figure 5.1: Arrangement of the 5 gold samples put in the HPGe detector for NAA.

The disc with the 5 samples was then exposed on the neutron flux on the 17<sup>th</sup> May 2022 at 17:30 up until 24<sup>th</sup> May 2022 at 15:45. Each sample was then put in the HPGe for Neutron Analysis Activation (NAA) after a time  $\Delta t_i$  from the finish of the exposure.

An important fact that need to be highlight is the concept already said at the end of Chapter 4. We have chosen 5 very thin gold samples in order to minimize the self-attenuation effect (4.4) as much as possible, and therefore to obtain a clean flux measurement.

## 5.2 Results

The examination of the  $\gamma$ -peaks showed us that the reaction with the neutron flux was:



where  $^{198}\text{Au}$  has a time decay of  $\tau_{\text{Au}} = 2.69d$  [5]. Knowing this, we can find the rate of activation  $\lambda_n^i$  for each sample following the same calculations already shown in subsection 3.1.2.

The cross section  $\sigma$  was evaluated by the plot data of Figure 3.1. In this case, we remember once again, that we knew *a priori* that the incident flux only contains the thermal part of neutrons ( $2,5 \cdot 10^{-8}$  MeV). Therefore we were interested only in a specific small region of the graph.

Knowing the rate of activation and the cross section, it is possible to compute the flux using equation 3.1.

Since we want to study the flux distribution in the different regions  $i$  on the disc, we can evaluate the percentage each flux differs from the centered one, defined as:

$$\frac{\phi^i}{\phi^1} = \frac{\lambda_n^i \sigma}{\lambda_n^1 \sigma} = \frac{\lambda_n^i}{\lambda_n^1} \quad (5.2)$$

All the obtained results are shown in Table 9.7.

This shows us that the neutron flux is indeed homogeneous on the whole surface of the disc within 9% error, where the propagation of errors is simply done with:

$$\delta\left(\frac{\phi^i}{\phi^1}\right) = \frac{\phi^i}{\phi^1} \sqrt{\left(\frac{\delta\lambda_n^i}{\lambda_n^i}\right)^2 + \left(\frac{\delta\lambda_n^1}{\lambda_n^1}\right)^2} \quad (5.3)$$

# Chapter 6

## FNG

14 MeV FNG, designed and built at ENEA in Frascati, is based on the fusion reaction



and produces up to  $10^{11}n/s$  continuously or pulsed.

FNG has been designed to carry out neutronic experiments in the context of European research on controlled thermonuclear fusion. The design of the blanket and shield of next generation fusion reactors requires an experimental verification of the nuclear cross sections used for the calculations as accurate as possible and a validation of the calculation methods used for the transport of neutrons. To do this, a special experimental activity called "benchmark experiments" is needed.

FNG uses a deuterium beam accelerated up to 300 keV against a tritium target to produce a nearly isotropic emission of 14 MeV neutrons by the 6.1 fusion reaction. Referring to Figure 6.1, the working principle is described below.

A beam of atomic and molecular deuterium ions is produced by a duoplasmatron type source (2) and cleaned by an analyzer magnet (4) through a  $90^\circ$  rotation.

In this way, only the atomic ions are injected into a constant gradient accelerator tube (5). The beam is then focused on the target through a trio of quadrupoles (7). The ion source, analyzer magnet, electronics and power supplies required for them are held at high voltage potential, housed in two different cabinets. The trio of quadrupoles, the vacuum system and the target are at ground potential. The regulation and current/voltage measurements of the various power supplies are carried out via a fiber optic connection up to the control room.



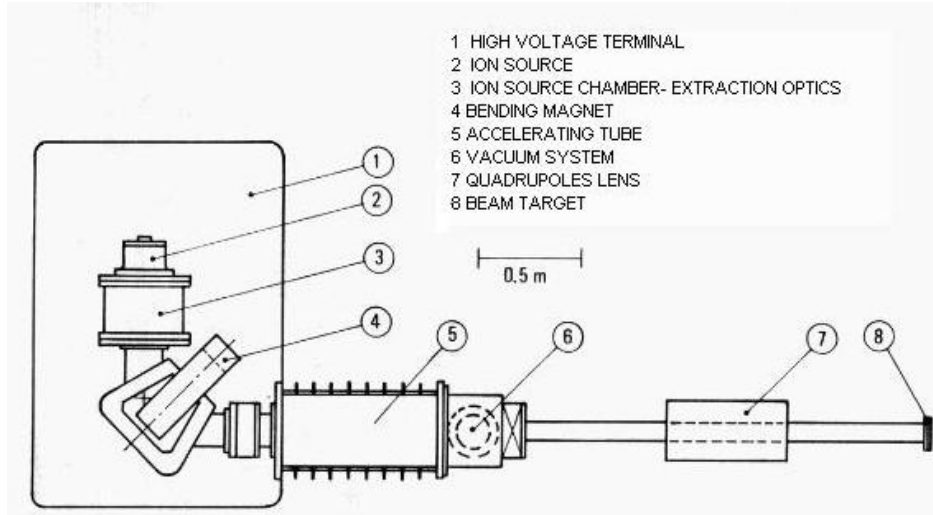


Figure 6.1: FNG view from above. [9]

During beam bombardment, tritium is released from the target towards the vacuum pumps. A tritium removal unit, housed in a glove box and located near the vacuum pumps, is used to purge the gas from the pump exhaust. Figure 6.2 provides a side view of the FNG.

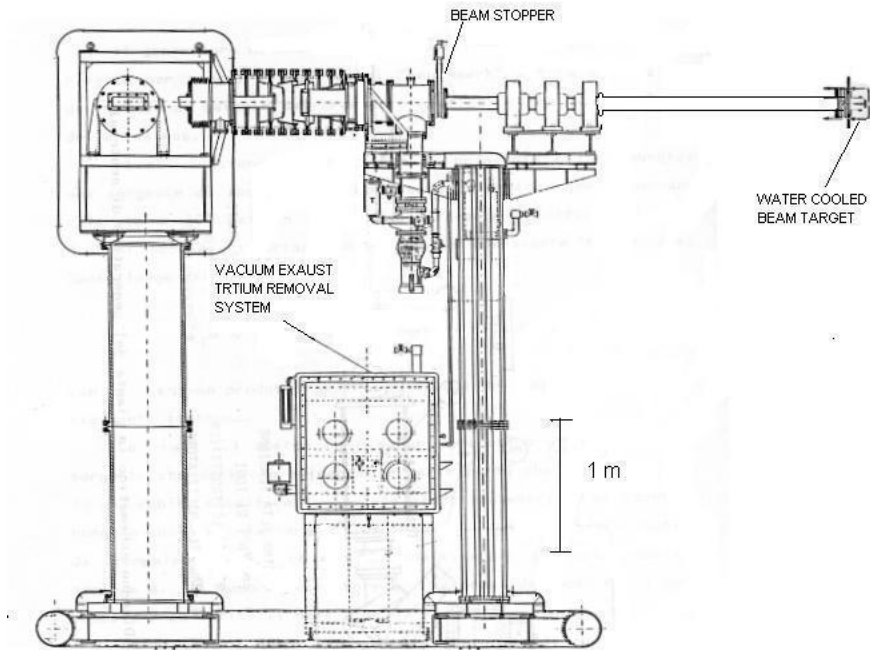


Figure 6.2: FNG side view. [9]

When it is necessary to produce 2.5 MeV neutrons, a *deuterated* target is mounted, instead of the *tritiated* one. The neutrons in this case are produced with the



fusion reaction. However, the intensity of the emission in this case, is one hundred times lower than that of 14 MeV, due to the smaller cross section of the D-D (6.2)

reaction. [9]

The current performances of FNG are collected in the table 6.1 below:

Beam energy [keV]	230
D+ beam current at the target [mA]	1
Beam spot at the target [mm]	10
Minimum distance from neutron source to expose samples [mm]	4
14 MeV neutron intensity on solid angle of $4\pi[s^{-1}]$	$10^{11}$
Tritiated target neutron output half-life time [h]	$\sim 25$
2.5 MeV neutron intensity on solid angle of $4\pi[s^{-1}]$	$\sim 10^8$
Neutron output monitor method	Associated particle

Table 6.1: Current performance parameters of the FNG..

FNG is housed in a large shielded hall ( $11.5 \times 12 \text{ m}^2$  and 9 m high) and the target is more than 4 m far from walls, floor and ceiling. This was done to reduce as much as possible neutron background coming from neutron reflection. Also the target holder was design very light, in order to reduce the contamination of the spectrum due to neutron scattering. Now we finally discuss the main topic of this report: the neutron generator and its flux to which a sample has been exposed.

As we said in Chapter 3, we used two different foils: one made of pure *Aluminium* and the other one made of pure *Niobium*. Their mass values were:  $m_{Al} = 0,78g$  and  $m_{Nb} = 2,167g$ .

## 6.1 Neutron Activation Analysis

### 6.1.1 Measurements

The foils were exposed for  $T = 3,83$  hours, considering the start of the exposure time  $t = 0$ .

After that, we have analyzed the gamma-ray energy spectrum produced by the foils in the HPGe.

#### NAA for Aluminium $^{27}\text{Al}$

Throughout the usual gamma spectroscopy we narrowed down the two only possible reactions the neutrons have made with  $^{27}\text{Al}$  to be:

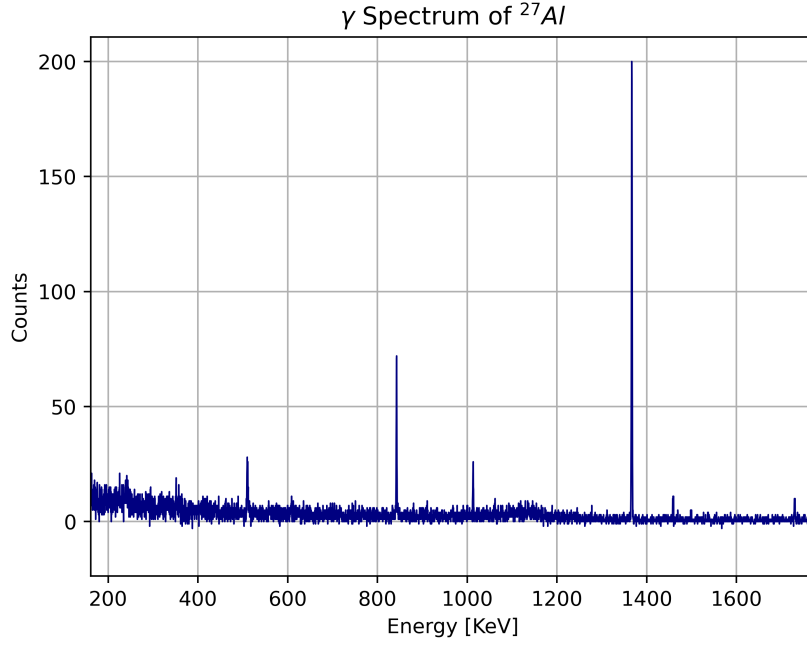


Figure 6.3: Gamma spectrum of activated  $^{27}\text{Al}$  in the relevant energy range  $160 \div 1750 \text{ keV}$ .



We measured the activity of  $^{27}\text{Mg}$  using the predominant peaks at 843 keV and 1014 keV. Using expressions 2.7 and 3.11, we have obtained

$$A^{27\text{Mg}}(t_{\text{Al}}) = (33 \pm 3) \text{ Bq} \quad (6.5)$$

and

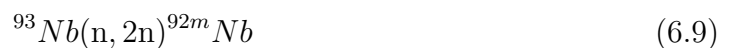
$$\lambda_n^{27\text{Al}} = (4.1 \pm 0.4) \cdot 10^{-21} \text{ s}^{-1} \quad (6.6)$$

given that the neutron flux is purely made out of 14 MeV neutrons, from [6] we obtain the cross section to be  $\sigma = 0.073$  barn and this gives one measurement, from  $^{27}\text{Al}$ , for the neutron flux to be:

$$\phi_{27\text{Al}} = (5.5 \pm 0.5) \cdot 10^4 \text{ cm}^{-2} \text{ s}^{-1} \quad (6.7)$$

### NAA for Niobium $^{93}\text{Nb}$

$^{93}\text{Nb}$  made the following reactions with the neutrons:



As we did in the subsection before, using expressions 2.7 and 3.11, we have obtained that for the relevant peaks at 202.5 keV and 479.3 keV the activity of  $^{90m}\text{Y}$ :

$$A^{90m\text{Y}}(t_{Nb}) = (93 \pm 30) Bq \quad (6.10)$$

and

$$\lambda_n^{93Nb} = (1.6 \pm 0.45) \cdot 10^{-22} s^{-1} \quad (6.11)$$

Which gives us, using from [6] the cross section  $\sigma = 0.0052$  barns, the neutron flux for  $^{90m}\text{Y}$ :

$$\phi_{93Nb} = (3.0 \pm 0.7) \cdot 10^4 cm^{-2} s^{-1} \quad (6.12)$$

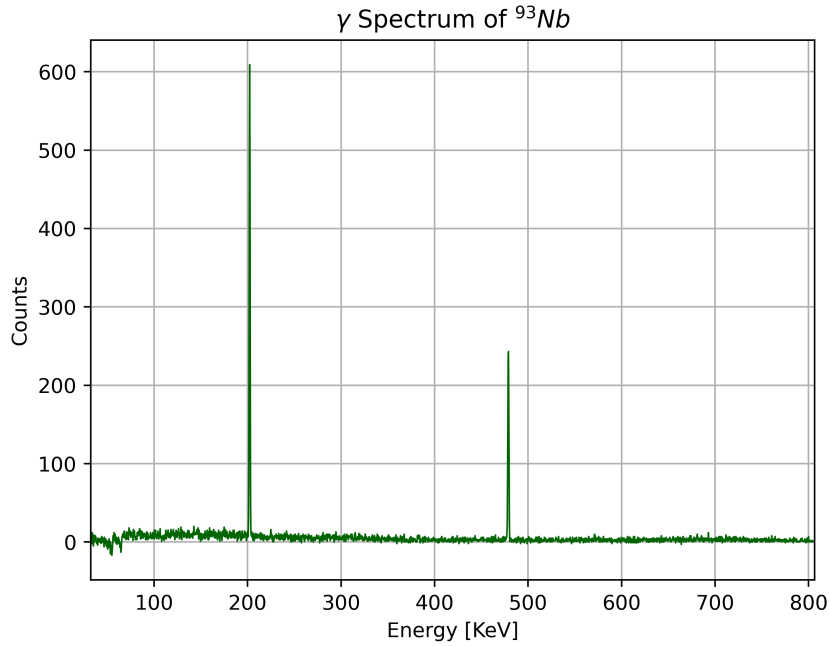


Figure 6.4: Gamma spectrum of activated  $^{93}\text{Nb}$  in the relevant energy range  $0 \div 800 \text{ keV}$ .

### The total flux

Having measured the rate of neutron activation, it is possible to find the neutron total flux:

$$\phi_{tot} = (4.3 \pm 1.3) \cdot 10^4 cm^{-2} s^{-1} \quad (6.13)$$

# Chapter 7

## Conclusions

A material that was exposed to neutrons can be put in a HPGe gamma-spectroscopy detector which, when is calibrated (see Section 2.1), is a perfect tool to find the energies of gamma photons from decay reactions. It is capable also of counting the number of photons during the measurement, therefore we can find the activity of a material with an error caused only due to the efficiency (see 2.6) and thickness of material (see Chapter 4). Having the activity we can measure the neutron flux on which the material was exposed (see Chapter 3).

In this paper we showed what happens to different atoms:  $^{27}\text{Al}$ ,  $^{93}\text{Nb}$ ,  $^{115}\text{In}$  and  $^{197}\text{Au}$  when we expose them to neutrons of energies of orders of  $25\text{ meV}$  (thermal neutrons),  $1\text{ MeV}$  and  $14.1\text{ MeV}$  (fast neutrons). Any neutron, with the energies mentioned, is capable of changing the internal structure of nucleus. When a neutron is captured or scattered, the atoms tend to go in a metastable element or start a decay chain reaction up until they reach a stable element. Some of them change completely their nuclear structure, like  $^{197}\text{Au}$  that decays into  $^{198}\text{Hg}$ , meanwhile others have a certain probability to maintain their nuclear structure with a certain probability, like  $^{115}\text{In}$ . Our materials were exposed to neutron fluxes of orders of  $10^3 \div 10^5\text{ cm}^{-2}\text{s}^{-1}$  for times of exposure of order of  $10 \div 100$  hours. We can expect the same reactions with these materials with less dense neutron fluxes and longer times of exposure. This gives us insight on what materials can be used to construct a strong and durable over time layer of a nuclear reactor, satellite, spaceship etc., because these are the type of constructions that are being exposed to different types of radiation, including the neutron radiation.

# Chapter 8

## Appendix

This short chapter is meant to clarify experimental measures in more detail. In particular it seems right to us, to explain how these two quantities have been estimated:

- Value of the energy peaks for the calibration of the HPGe detector
- $N_{measured}$  counts for the computation of efficiency
- Effective cross section  $\sigma$  for a specific energy range

### 8.1 Energy peaks

Section 2.1 of Chapter 2 has been devoted to the description of HPGe calibration. In order to find the conversion factor between channel and energy, data analysis of the gamma spectrum of each source is required where the spectrum is provided by the software [3]. Below we report the example of the data analysis of  $^{137}\text{Cs}$  sample. In Figure 8.1 is reported the  $\gamma$  spectrum of  $^{137}\text{Cs}$ .

$$A + n \rightarrow B \rightarrow C + \gamma \text{ (rilevato da HPGe)} \quad (8.1)$$

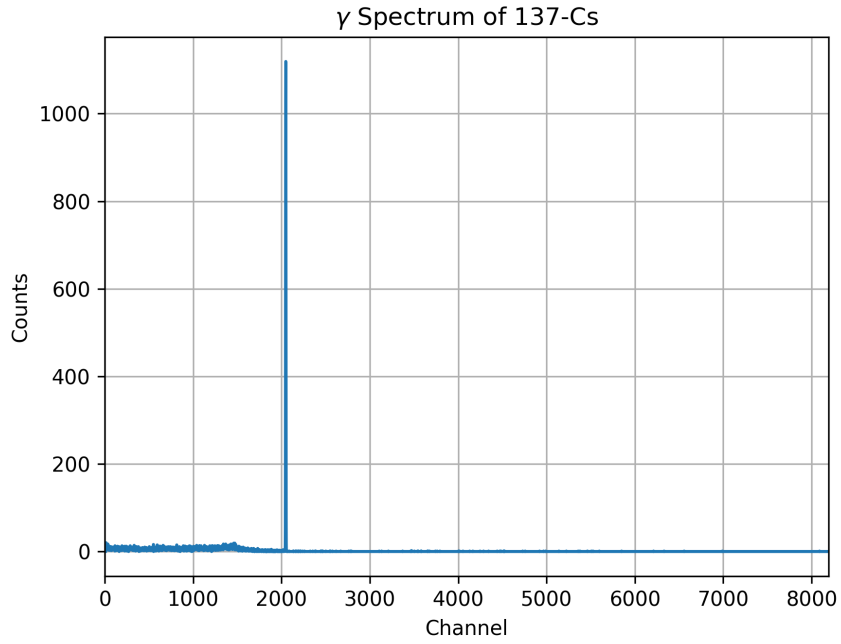


Figure 8.1:  $\gamma$  spectrum of  $^{137}\text{Cs}$ . The range of the x-axis is the maximum detectable by the software.

It is evident that for  $^{137}\text{Cs}$  there is one single peak to consider. If we now focus on the single peak, we can see how the counts are distributed in a normal way around a single channel value (Figure 8.2):

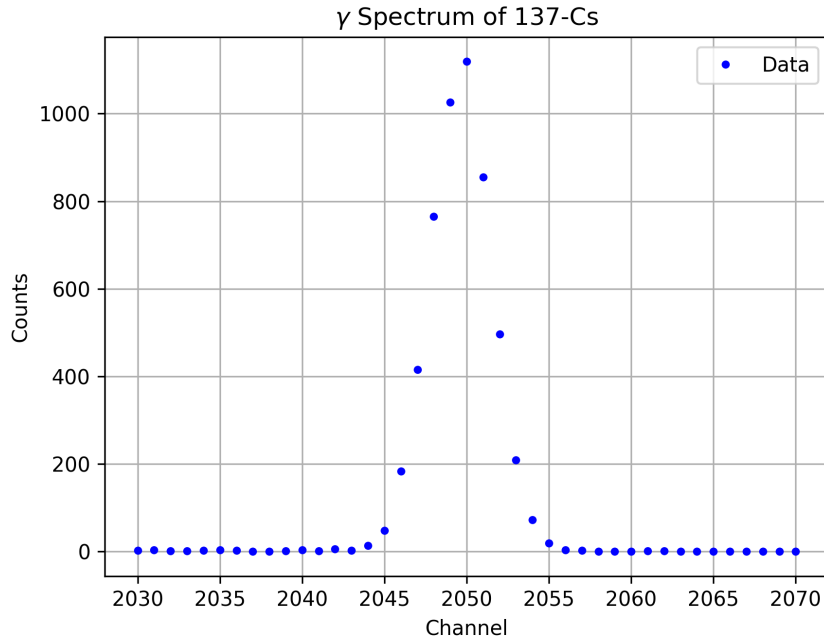


Figure 8.2: Focus on  $^{137}\text{Cs}$  peak. Counts are distributed normally around a single value.

Therefore it's possible to perform a gaussian fit of these data in order to extract

the exact value of the channel (Figure 8.3). For a better comprehension of the fit's parameters, we write below the equation used for data's interpolation:

$$pdf(x) = H + Ae^{-\frac{(x - \mu)^2}{2\sigma^2}} \quad (8.2)$$

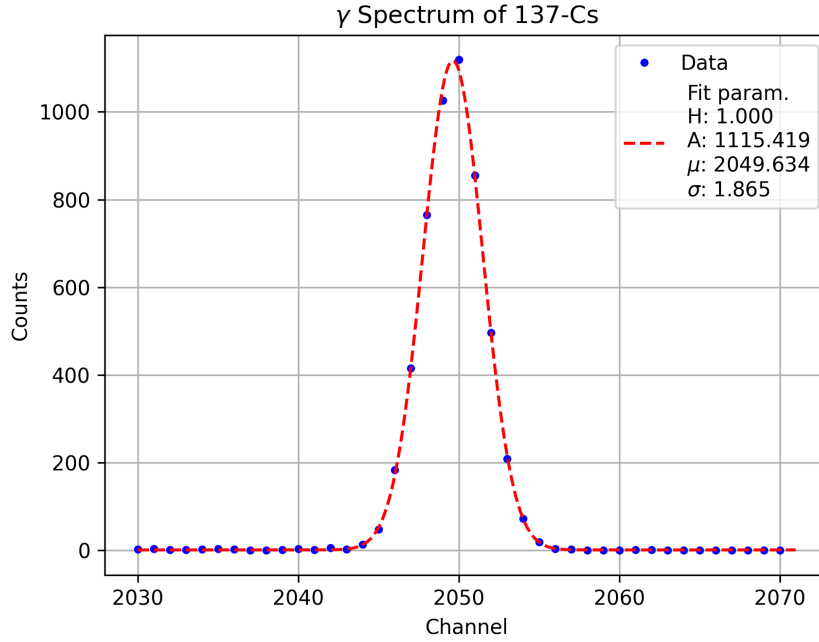


Figure 8.3: Focus on  $^{137}\text{Cs}$  peak. Data are interpolated by a gaussian fit in order to extract the average value. All the letters of fit's parameters refer to equation 8.2.

So, for the peak of  $^{137}\text{Cs}$  we can associate a channel value equal to  $2049,63 \pm 1,86$ . The same procedure was used for all the other samples (and the relative peaks) mentioned in section 2.1.

## 8.2 Evaluation of Efficiency

Section 2.2 of Chapter 2 has been devoted to the evaluation of the HPGe detector's efficiency with two different thickness configurations via equation 2.7. We want to focus on how the  $N_{measured}$  quantity was estimated.

Essentially we can define the  $N_{measured}$  as the sum of significant counts under a peak. The question is to give a concrete meaning to the word "significant".



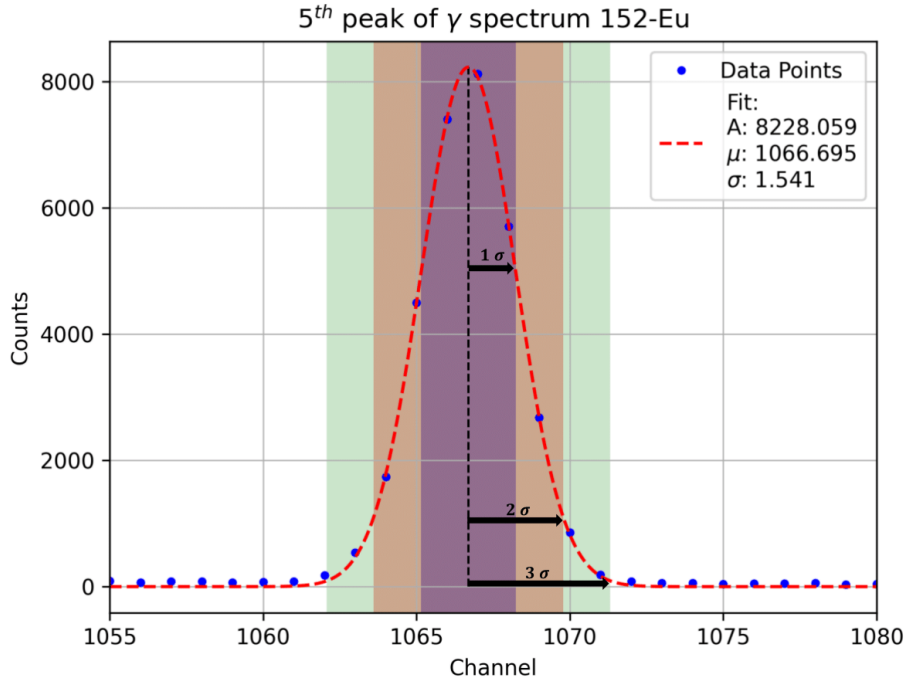


Figure 8.4: Focus on 5<sup>th</sup>  $^{152}\text{Eu}$  peak. In the graph are highlighted the regions with an increase of  $1\sigma$ .

Figure 8.4 shows a focus on the fifth peak of the  $\gamma$  spectrum of  $^{152}\text{Eu}$ . As already described in section 8.1 a Gaussian fit was performed on the data. With the aim of covering the whole area of the Gaussian and, therefore, to make the error that may result from the total count negligible, we have chosen to consider the counts in the range  $\mu \pm 3\sigma$ . All the points outside the last highlighted region are excluded from the count.

## 8.3 Effective Cross Section

In several sections we need to evaluate the effective cross section of neutron interactions with different nuclides to measure the flux of neutrons (see 3.4). We take two different approaches to evaluating the thermal cross section and the fast cross section.

### 8.3.1 Thermal Cross Section

Thermal neutrons can be described as a gas of free neutrons with a fixed energy  $E = k_b T$ , where  $T$  is the ambient temperature. In our case  $T$  is the room temperature and so the neutrons have an energy of  $0.025\text{meV}$ .

This means that the effective thermal cross section will be considered exact at that energy.

### 8.3.2 Fast Cross Section

Since the energy of fast neutrons is in the range 1 *MeV* to 2 *MeV*. We will define the effective cross section to be:

$$\sigma_f = \sum_E^N \frac{\sigma(E)}{N} = \frac{\sigma(1\text{MeV}) + \sigma(2\text{MeV})}{2} \quad (8.3)$$

and the standard deviation to be:

$$dev(\sigma_f) = \sqrt{\frac{\sum_E^N (\sigma(E) - \sigma)^2}{N}} = \frac{|\sigma(1\text{MeV}) - \sigma(2\text{MeV})|}{2} \quad (8.4)$$

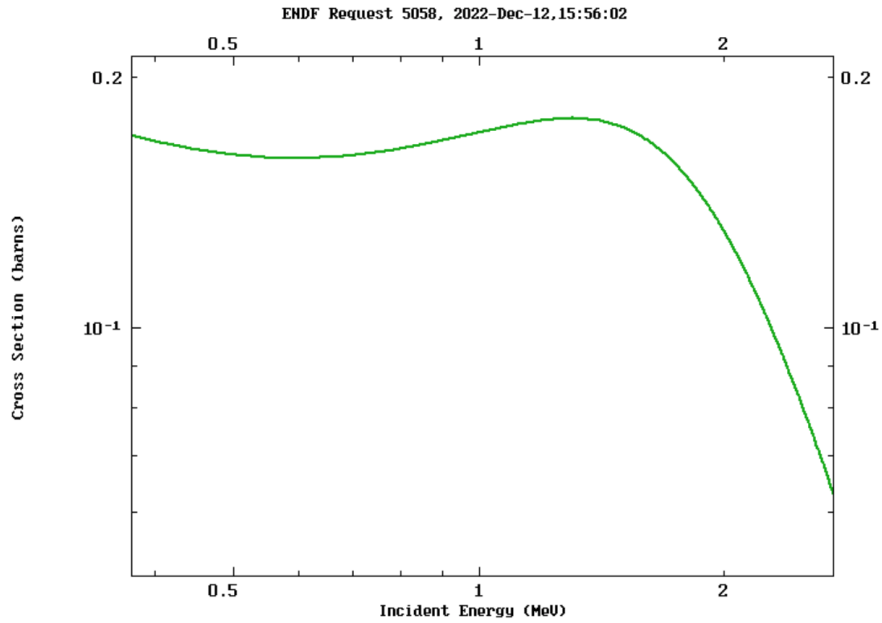


Figure 8.5: An example of calculation can be found in the neutron activation of  $^{115}\text{In}(n,g)^{116m1}\text{In}$ : where we extrapolate  $\sigma(1\text{MeV}) = 0.17$  barns and  $\sigma(2\text{MeV}) = 0.15$  barns, which gives us the effective cross section to be  $\sigma_f = (0.16 \pm 0.01)$  barns

# Chapter 9

## Tables

<sup>152</sup> Eu - 10 cm					
A [Bq]	Δt [s]	Y	Energy[keV]	Efficiency	Error
10800	873,83	0,286	121,78	0,01275	0,00006
//	//	0,076	244,69	0,0104	0,0001
//	//	0,023	411,12	0,0064	0,0002
//	//	0,028	443,98	0,0065	0,0002
//	//	0,129	778,90	0,00450	0,00006
//	//	0,042	867,39	0,0041	0,0001
//	//	0,146	964,13	0,00404	0,00005
//	//	0,102	1084,00	0,00352	0,00006
//	//	0,136	1112,11	0,00345	0,00005
//	//	0,014	1212,95	0,0029	0,0002
//	//	0,016	1299,14	0,0031	0,0001
//	//	0,210	1408,01	0,00295	0,00004
<sup>133</sup> Ba - 10 cm					
A [Bq]	Δt [s]	Y	Energy[keV]	Efficiency	Error
6320	352,72	0,02	53,161	0,0079	0,0004
//	//	0,34	80,99	0,0107	0,0001
//	//	0,07	276,39	0,0095	0,0002
//	//	0,18	302,85	0,0083	0,0001
//	//	0,62	356,02	0,00745	0,00007
//	//	0,09	383,85	0,0071	0,0002

Table 9.1: Data for efficiency of HPGe detector with 10 cm of thickness

$^{152}\text{Eu}$ - 6 cm					
A [Bq]	$\Delta t$ [s]	Y	Energy[keV]	Efficiency	Error
10800	786,76	0,286	121,78	0,02407	0,00009
//	//	0,129	778,90	0,00789	0,00008
//	//	0,042	867,39	0,0079	0,0001
//	//	0,146	964,13	0,00673	0,00007
//	//	0,102	1084,00	0,00636	0,00008
//	//	0,136	1112,11	0,00638	0,00007
//	//	0,014	1212,95	0,0068	0,0002
//	//	0,016	1299,14	0,0056	0,0002
//	//	0,210	1408,01	0,00513	0,00005
$^{133}\text{Ba}$ - 6 cm					
A [Bq]	$\Delta t$ [s]	Y	Energy[keV]	Efficiency	Error
6320	189,15	0,02	53,161	0,0178	0,0008
//	//	0,34	80,99	0,0197	0,0002
//	//	0,07	276,39	0,0166	0,0004
//	//	0,18	302,85	0,0151	0,0002
//	//	0,62	356,02	0,0137	0,0001
//	//	0,09	383,85	0,0133	0,0003

Table 9.2: Data for efficiency of HPGe detector with 6 cm of thickness

$^{116m}\text{In}$							
Thin		Medium		Thick A		Thick B	
Mass [g]	Thickness [mm]	Mass	Thickness	Mass	Thickness	Mass	Thickness
1,90	1	3,61	2	8,86	5	8,67	5

Table 9.3: Features of the four  $^{116m}\text{In}$  foils. The units of measurement for mass and thickness are all the same.

E=416 KeV		E=818 KeV		E=1097 KeV		E=1293 KeV	
A/m [Bq/g]	Thickn.[mm]	A/m	Thickn.	A/m	Thickn.	A/m	Thickn.
1064,877	1	1077,219	1	790,695	1	1061,331	5
876,417	2	832,116	2	646,106	2	871,473	5
563,85	5	509,588	5	419,142	5	600,892	5
454,227	5	472,834	5	355,376	5	488,610	5
380,952	6	387,580	6	295,933	6	416,357	5
338,143	7	376,564	7	273,880	7	375,708	5
253,132	10	283,319	10	209,299	10	285,540	5
217,520	11	236,645	11	184,613	11	241,937	5
178,573	12	170,507	12	149,541	12	204,614	5

Table 9.4: Data which refers to Figure 4.1. The units of measurements for  $A/m$  and Thickness are all the same.

E=416 KeV	E=818 KeV	E=1097 KeV	E=1293 KeV
$\mu \pm \sigma$	$\mu \pm \sigma$	$\mu \pm \sigma$	$\mu \pm \sigma$
0,1768 $\pm$ 0,0001	0,1704 $\pm$ 0,0001	0,1637 $\pm$ 0,0001	0,1591 $\pm$ 0,0001

Table 9.5: Attenuation coefficient values with relative errors

Golden Samples $^{197}\text{Au}$				
Label	r[cm]	$\theta[^\circ]$	mass[g]	error
1	0	0	0,368	0,001
2	10	0	0,287	0,001
3	10	270	0,256	0,001
4	10	180	0,251	0,001
5	10	90	0,257	0,001

Table 9.6: Data and coordinates of samples used for the study of neutron flux distribution

Golden Samples $^{197}\text{Au}$					
Label	$\Delta t_i[\text{min}]$	$\lambda_n^i[\text{aHz}]$	$\sigma_{\text{Th}}[\text{b}]$	$\phi^i/\phi^1$	error[%]
1	9	$43 \pm 2$	95	1	9
2	22	$43 \pm 2$	95	1	9
3	33	$44 \pm 2$	95	0,97	9
4	44	$43 \pm 2$	95	1	9
5	55	$43 \pm 2$	95	1	9

Table 9.7: The neutron flux distribution in different regions of the disc. The prefix *aHz* stands for *attoHertz* equal to  $10^{-18}\text{Hz}$ .

# Chapter 10

## Glossary

$^{197}\text{Au}$ Gold-197	$\gamma$ Photon
$^{198}\text{Au}$ Gold-198	$I$ Intensity
$^{60}\text{Co}$ Cobalt-60	$E$ Energy
$^{137}\text{Cs}$ Cesium-137	$r$ Radius
$^{152}\text{Eu}$ Europium-152	$d$ Diameter
$^{133}\text{Ba}$ Barium-133	$\rho$ Density
$^{115}\text{In}$ Indium-115	$\sigma$ Cross section
$^{116m}\text{In}$ Indium-116m	$\sigma_{th}$ Thermal cross section
$^{237}\text{Np}$ Neptunium-237	$\sigma_f$ Fast cross section
$^{198}\text{Hg}$ Mercury-198	$\phi$ Flux
$^2\text{H}$ Deuterium	$\mu$ Attenuation coefficient
$^3\text{H}$ Tritium	$C_{att}$ Self attenuation coefficient
$A$ Activity	$n$ Neutron
$t$ Time	$\tau$ Time of decay
$\epsilon$ Efficiency	$\lambda$ Rate of activation
$Y$ Yield of a peak	

# Bibliography

- [1] Guido Van Rossum and Fred L. Drake. *Python 3 Reference Manual*. CreateSpace, Scotts Valley, CA, 2009.
- [2] John R Lamarsh. *Introduction to nuclear reactor theory*. Addison-Wesley, 1966.
- [3] Ametek Ortec. *GammaVision Gamma Spectroscopy*. 2020.
- [4] Glenn F Knoll. *Radiation detection and measurement*. John Wiley & Sons, 2010.
- [5] L.P. Ekström S.Y.F. Chu and R.B. Firestone. The lund/lbnl nuclear data search. <http://nucleardata.nuclear.lu.se/toi/index.asp>, 1999.
- [6] Evaluated nuclear data file: Data source: Iaea-nds, wpec, csewg, ippe, cndc, jaea, nrg, ccfe, fzk. <https://www-nds.iaea.org/exfor/endl.htm>, 2022.
- [7] AJJ Bos. High sensitivity thermoluminescence dosimetry. *Nuclear Instruments and Methods in Physics Research Section B: Beam Interactions with Materials and Atoms*, 184(1-2):3–28, 2001.
- [8] Physical Measurement Laboratory of the National Institute of Standards and Technology (NIST). Security requirements for cryptographic modules, u.s. department of commerce. <https://www.nist.gov/pml>, Washington D.C., 2001.
- [9] Enea - unità tecnica fusione. <http://www.fusione.enea.it/index.html.en>, Centro Ricerche FRASCATI (Roma), Via Enrico Fermi 45, 00044 - Frascati (RM) Italy, 2000-2010.
- [10] Leslie Lamport. *TEX: a Document Preparation System*. Addison Wesley, Massachusetts, 2 edition, 1994.